SCIENTIFIC REPORTS

OPEN

Dielectric Jump and Negative Electrostriction in Metallosupramolecular Ionic Crystals

Received: 4 November 2017
Accepted: 22 January 2018
Published online: 08 February 2018

Satoshi Yamashita, Yasuhiro Nakazawa, Shusuke Yamanaka, Mitsutaka Okumura, Tatsuhiro Kojima, Nobuto Yoshinari & Takumi Konno

In natural ionic solids, cationic and anionic species are alternately arranged to minimize electrostatic energy. Aggregation of identical ionic species is commonly prohibited due to the repulsive, long-range nature of Coulombic interactions. Recently, we synthesized unique ionic solids, $[Au^{I}_4Co^{III}_2(dppe)_2(D\text{-}pen)_4]X_2{\cdot}nH_2O$ (dppe = 1,2-bis(diphenylphosphino)ethane, D-pen = D-penicillaminate), in which complex cations are self-assembled into a cationic supramolecular octahedron, while monovalent or divalent inorganic anions are aggregated into an anomalous anionic cluster accommodating several water molecules. This quite unusual aggregation manner originates from various molecular-level non-Coulombic interactions such as hydrogen bonds and CH-π interactions; thus, this class of ionic solids is referred to as non-Coulombic ionic solids, abbreviated as NCISs. Herein, we report that the NCISs with a peculiar charge-separated (CS) structure in a cubic lattice show a negative, isotropic electrostriction phenomenon that has never been found in any ionic solids, as well as an anomalously large relaxer-like dielectric jump phenomenon reaching to an application level of $\varepsilon'/\varepsilon_0 \sim 10^5$. The appearance of these phenomena was explained by the cooperative dynamics of inorganic anions and dipolar water molecules in the pliable anionic clusters that are surrounded by a rather robust cationic metallosupramolecular framework with a meso-scopic scale.

It has been recognized that a variety of polynuclear and supramolecular coordination compounds are created from thiol-containing amino acids, such as L-cysteine (L-H_2cys), D-penicillamine (D-H_2pen), and their derivatives, in combination with 3d and 4d transition metal ions, because these amino acids can adopt various coordination modes to multiple metal centres by using amine, carboxyl, and/or thiol groups dependent on their protonation/deprotonation states[1–4]. We found that the introduction of hydrophobic dppe (1,2-bis(diphenylphosphino)ethane) into a gold(I)-cobalt(III) coordination system with hydrophilic D-pen affords a cationic $Au^{I}_4Co^{III}_2$ hexanuclear complex, $[Au_4Co_2(dppe)_2(D\text{-}pen)_4]^{2+}$ ($[\mathbf{1}]^{2+}$), in which two Co^{III} centres are spanned by two $[Au^{I}_2(dppe)(D\text{-}pen)_2]^{2-}$ linkers[1–3]. On crystallization with appropriate monovalent inorganic anions, such as ClO_4^-, NO_3^-, and Cl^- or divalent anions such as SiF_6^{2-} and SO_4^{2-}, the 6 $Au^{I}_4Co^{III}_2$ cations of $[\mathbf{1}]^{2+}$ are self-assembled to form huge cationic supramolecular octahedrons, $\{[\mathbf{1}]^{2+}\}_6$, which are closely packed into a face centred cubic (fcc) structure with a lattice parameter of $a \approx 3.8$ nm. The mesoscopic-scale fcc structure involves large hydrophilic and hydrophobic tetrahedral interstitial spaces with volumes of ~900 Å^3 and ~1500 Å^3, respectively, besides small octahedral interstitial spaces with a volume of ~70 Å^3. In each hydrophilic tetrahedral interstice, 10 monovalent anions or 6 divalent anions are aggregated in adamantane-like $\{X^-\}_{10}$ or octahedron-like $\{X^{2-}\}_6$ cluster structures, together with several water molecules. On the other hand, each hydrophobic tetrahedral interstice is occupied by a number of water molecules to form a huge water cluster, which works as a reservoir of water molecules in the crystal. As a consequence of the delicate balance of condensation energies, the cationic supramolecular octahedrons and the inorganic anion clusters are alternately arranged in the crystal, constructing a giant zinc-blend-like lattice structure with a large charge-separation state. In this class of ionic solids, which is referred to as charge-separation type non-Coulombic ionic solids (CS-NCISs) (Fig. 1), the cationic framework

Department of Chemistry, Graduate School of Science, Osaka University, Machinakeyama 1-1, Toyonaka, Osaka, 560-0043, Japan. Correspondence and requests for materials should be addressed to Y.N. (email: nakazawa@chem.sci.osaka-u.ac.jp) or T.K. (email: konno@chem.sci.osaka-u.ac.jp)

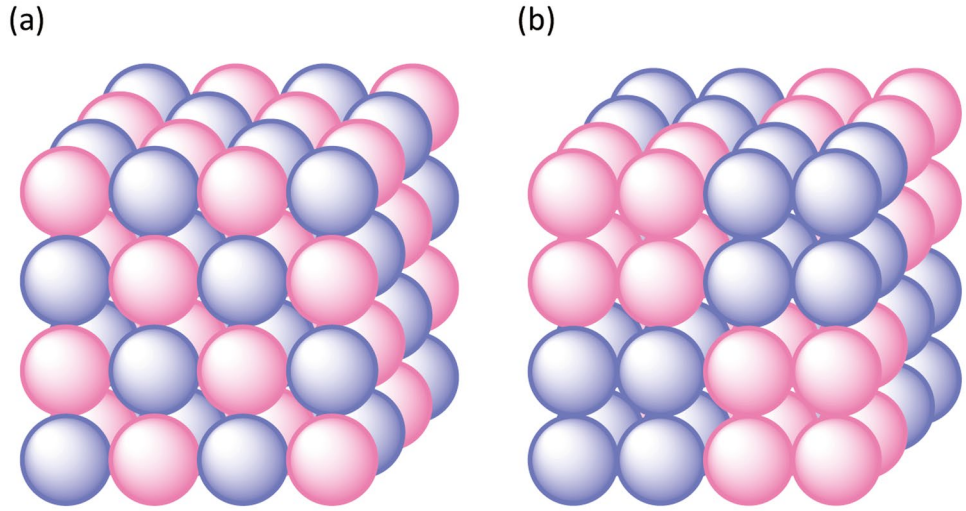

Figure 1. (**a**) Schematic illustration of (**a**) common and (**b**) charge-separation type non-Coulombic ionic solid (CS-NCIS) materials. Red and blue balls represent cationic and anionic species.

consisting of the supramolecular octahedrons is rather robust even at a high temperature, whereas the portion of the anionic clusters composed of inorganic anions and water molecules appears to be quite flexible. Such being the case, the deformation of the local structure by external stimuli, especially by electric fields, possibly induces unexpected changes in the dielectric and elastic properties through the coupling of charge and lattice degrees of freedom with retaining the framework. Throughout systematic experiments and analyses using single crystals of the CS-NCISs, we found not only an extraordinary large relaxer-like dielectric jump in a symmetric cubic crystal system but also an unprecedented lattice contraction upon the application of electric fields. Herein, we wish to report these remarkable discoveries that have never been found in metal-organic ionic solids.

Previously, the crystal structures of [**1**]$X_2{\cdot}nH_2O$ [$X_2 = Cl_2$, Br_2, $(NO_3)_2$, $(ClO_4)_2$, SO_4, SiF_6] were investigated using a laboratory X-ray source at 200 K[2,3]. However, the positions of the water molecules were not clearly determined owing to the limited data quality and their disordered structure. That is, for [**1**]$(ClO_4)_2{\cdot}nH_2O$ and [**1**]$(NO_3)_2{\cdot}nH_2O$, no water molecules were found in the anionic cluster that existed in each hydrophilic tetrahedral interstice, although several water molecules were observed for [**1**]$Cl_2{\cdot}nH_2O$, [**1**]$Br_2{\cdot}nH_2O$, [**1**]$(SO_4){\cdot}nH_2O$, and [**1**]$(SiF_6){\cdot}nH_2O$. In addition, water molecules that existed in the hydrophilic tetrahedral interstices could not be modelled for all [**1**]$X_2{\cdot}nH_2O$. In this work, the crystal data of [**1**]$X_2{\cdot}nH_2O$ were collected using synchrotron X-ray radiation at 100 K to determine the positions of the water molecules and inorganic anions more precisely.

The synchrotron single-crystal X-ray analysis of [**1**]$(ClO_4)_2{\cdot}nH_2O$ clearly indicated the presence of 2 water molecules that are disordered inside the adamantane-like $\{ClO_4^-\}_{10}$ cluster, although the overall crystal structure is essentially the same as that determined previously (Fig. 2). Moreover, 4 water molecules that are also disordered were found on the surface of the $\{ClO_4^-\}_{10}$ cluster. These water molecules appear to moderate the Coulombic repulsion between ClO_4^- ions in the cluster. This is also the case for [**1**]$(NO_3)_2{\cdot}nH_2O$; two water molecules that are disordered were found inside the adamantane-like $\{NO_3^-\}_{10}$ cluster (Fig. S1). In this case, however, 4 of 10 nitrate anions, which are located at the tetrahedral site of the adamantane, are disordered over two positions. This disorder makes it difficult to determine the positions of water molecules located on the surface of the $\{NO_3^-\}_{10}$ cluster. The numbers and the positions of water molecules inside and on the surface of the inorganic-anion cluster were precisely determined for the other [**1**]$X_2{\cdot}nH_2O$; [**1**]$Cl_2{\cdot}nH_2O$ and [**1**]$Br_2{\cdot}nH_2O$ each accommodate 4 water molecules inside the adamantane-like $\{X^-\}_{10}$ cluster and 12 water molecules on the surface of the $\{X^-\}_{10}$ cluster, whereas [**1**]$(SO_4){\cdot}nH_2O$ and [**1**]$(SiF_6){\cdot}nH_2O$ each accommodate 4 water molecules inside the octahedron-like $\{X^{2-}\}_6$ cluster and 4 water molecules on the surface of the $\{X^{2-}\}_6$ cluster (Fig. S1). In addition, a large water cluster that consists of more than 36 water molecules, some of which are disordered, was commonly found for all [**1**]$X_2{\cdot}nH_2O$ in each hydrophobic tetrahedral interstice (Figs 2 and S1). The synchrotron X-ray analysis was also carried out at a higher temperature for [**1**]$(NO_3)_2{\cdot}nD_2O$, which demonstrated the thorough retention of its crystallinity even at 370 K (Fig. S2). The molecular structure of $[\mathbf{1}]^{2+}$ and its special arrangement in the crystal at 370 K are essentially the same as those at 100 K. However, a slight contraction of the $\{NO_3^-\}_{10}$ cluster, together with the directional change of each NO_3^- anion, was observed by increasing the temperature; the average N … N distances are 4.72 Å and 4.63 Å at 100 K and 370 K, respectively. In addition, most of the water molecules were not found from the difference Fourier map at 370 K, presumably due to the severe dynamic disorder of water molecules in the crystal. These observations suggest a high motility of inorganic anions and water molecules accommodated in the rigid supramolecular framework composed of $[\mathbf{1}]^{2+}$.

To gain more insight into the thermal stability of the CS-type NCISs, the temperature dependency of the heat capacity (C_p) was measured for [**1**]$(ClO_4)_2{\cdot}nH_2O$ (Fig. 3a). There are no significant thermal anomalies in the temperature range of 2.0 K–240 K. This clearly indicates that the structure with the cubic space group of *F*23 is stable in this temperature range; the structural deformation to monoclinic or triclinic phases does not occur despite the drastic charge-separation state of [**1**]$(ClO_4)_2{\cdot}nH_2O$ in the crystal. The crystal stability up to 450 K was also

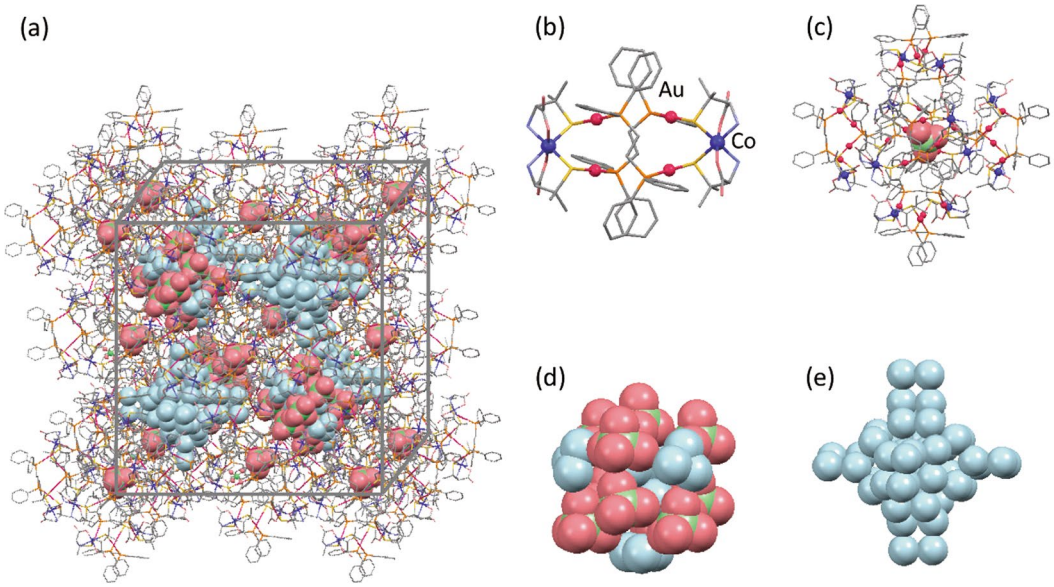

Figure 2. Structures of (**a**) packing, (**b**) complex-cation, (**c**) cationic supramolecular octahedron, (**d**) inorganic-anion cluster, and (**e**) water cluster in [**1**]$(ClO_4)_2 \cdot nH_2O$.

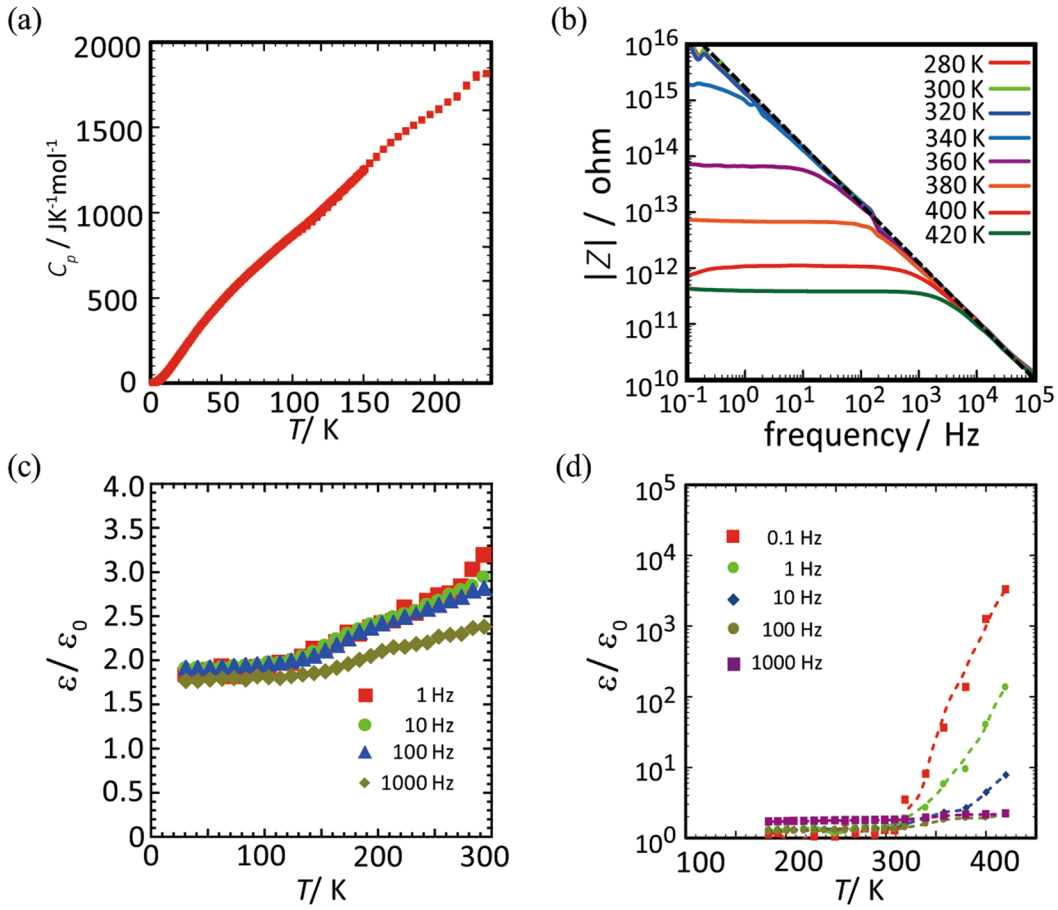

Figure 3. (**a**) Temperature dependence of the heat capacity of [**1**]$(ClO_4)_2 \cdot nH_2O$. (**b**) Temperature and frequency dependences of the absolute value of the complex ac impedance of [**1**]$(ClO_4)_2 \cdot nH_2O$. The dashed lines in the figure show a para-electric state corresponding to a dielectric constant ($\varepsilon'/\varepsilon_0$) of 1.5–3.0. (**c**) The temperature dependence of the real part of $\varepsilon'/\varepsilon_0$ for [**1**]$(ClO_4)_2 \cdot nH_2O$ between 30 K and 300 K. (**d**) The temperature dependence of the real part of $\varepsilon'/\varepsilon_0$ for [**1**]$(ClO_4)_2 \cdot nH_2O$ between 180 K and 420 K in logarithmic plot.

confirmed by the differential thermal analysis (DTA); no structural phase transition and decomposition peaks were observed up to this temperature, although the release of water molecules was detected by the thermogravimetry analysis (TGA) above 380 K (Fig. S3). The release of water molecules was prohibited when the crystal surface was coated by an epoxy resin. Note that the C_p values increase monotonously with the temperature, even above 200 K (Fig. 3a). This implies that the heat capacity does not obey the typical Debye feature presumably because of the significant contribution of optical phonon modes that originate from the translational and rotational motions of small molecules (H_2O and/or inorganic anions) in the interstitial spaces with increasing temperature.

Figure 3b shows the frequency (ω) dependency of the absolute values of the ac impedance, Z, in the temperature range from 280 K to 420 K for a single-crystal of [**1**]$(ClO_4)_2{\cdot}nH_2O$. In the low temperature region, $\log|Z|$ obeys a linear relation with $\log\omega$ in the wide frequency region between 10^{-1} Hz and 10^5 Hz. This means that the capacitance values are nearly constant. Moreover, the real part of the relative permittivity ($\varepsilon_r = \varepsilon'/\varepsilon_o$) is within a range of 1.5–3.0, which is on the same order as insulating materials, such as SiO_2 glasses, quartz, and sapphire (Fig. 3c,d)[5,6]. However, the relative permittivity changes abruptly just above room temperature with a kink feature in $\log|Z|$ (Fig. 3b). While the deformation of crystal symmetry with increasing temperature has generally been observed for ferroelectric transition metal oxides such as $BaTiO_3$ (BTO)[6] and $K(NH_4)_2PO_4$ (KDP)[7] and organic charge-transfer complexes such as TTF-CA[8,9], no deformation was noticed for [**1**]$(ClO_4)_2{\cdot}nH_2O$. The abrupt increase of the $\varepsilon'/\varepsilon_0$ values is commonly observed for the other CS-NCISs having different anionic clusters, [**1**]$X_2{\cdot}nH_2O$ ($X_2 = (NO_3)_2$, Cl_2, Br_2, SO_4, SiF_6), although the temperature and magnitude are dependent on the type of anion included (Fig. 4). The $\varepsilon'/\varepsilon_0$ values at 10^{-1} Hz for these compounds reach to 10^3–10^5, except for [**1**]$(SO_4){\cdot}nH_2O$; these values are in the highest class among those found in various molecule-based dielectric compounds and are comparable with those reported in the relaxer systems of some functional ceramics[9,10]. The observed temperature dependency of $\varepsilon'/\varepsilon_0$ indicates that this permittivity jump is dominated by an activation-type of dynamics. The evaluation of the onset temperature of the permittivity jump at various frequencies revealed the nearly linear relation in $\log\omega$ vs. $1/T_{onset}$. From this relation, the activation energies are estimated to be 50–100 kJ mol^{-1} (Fig. S4), which are on a similar order to those found in relaxers such as $BaTiO_3$ (BTO) and $Pb(Mg_{1-x}Nb_x)O_3$ (PMN)-based compounds[10,11]. Note that the gradual increase of $\varepsilon'/\varepsilon_0$ for [**1**]$(ClO_4)_2{\cdot}nH_2O$ starts from 150–160 K as a precursor of the abrupt jump (Fig. 3c). Since this temperature range is close to the glass transition temperature of supercooled water embedded in nano-porous or polymer systems[12–15], the dielectric behaviour for [**1**]$(ClO_4)_2{\cdot}nH_2O$ is most likely due to the molecular dynamics triggered by dipolar water molecules existing in the anionic cluster of $\{ClO_4^-\}_{10}$. It has been recognized that water molecules confined in nano-pores can form a supercooled liquid state to give a rather large dielectric response[16,17]. However, such dynamics in a metastable liquid state has been realized only in wet conditions obtained by exposing framework materials to water. Thus, the dielectric dynamics realized for the CS-NCISs ([**1**]$X_2{\cdot}nH_2O$) under non-wet conditions is a significant aspect of the phenomena to be emphasized.

To inspect the dynamic behaviour of the anionic clusters accommodating water molecules, we performed molecular dynamics (MD) calculations with a quantum mechanics (QM)/molecular mechanics (MM) model for [**1**]$Cl_2{\cdot}nH_2O$ at 300 K. Figure 5a illustrates the equivalued surfaces of the probability densities for Cl^- anions and O and H atoms ($\rho(X) = 0.005$, X = Cl^-, O, H) as wire meshes. The X-ray structure positions for Cl^- anions, water molecules, and other molecules are also shown in the sphere, stick, and wire models, respectively. From this figure, it is seen that the positions of Cl^- anions are rather stable at room temperature, while the water molecules fluctuate considerably but remain bound to the anionic cluster to moderate the repulsive interaction between Cl^- anions. This situation allows them to have a liquid-like feature at approximately room temperature. Therefore, it is assumed that the frequency-dependent motion of dipolar water molecules induced by ac electric fields is a trigger for the dielectric jump, as in the case of water molecules in nano-porous systems[18,19]. The calculations also supported that the liquid-like dynamics of water molecules in the cluster can induce the structural distortion of the whole anionic cluster. This cooperative effect accounts for the unexpectedly large dielectric jump phenomenon in the CS-NCISs of [**1**]$X_2{\cdot}nH_2O$. In addition, the anion dependency on the dielectric features is understood by the difference in the rigidity of water molecules accommodated in the anionic cluster. That is, [**1**]$Cl_2{\cdot}nH_2O$ that contains the anion clusters of $\{Cl^-\}_{10}$ with a sparse structure shows the most sensitive relaxer feature, whereas [**1**]$(ClO_4)_2{\cdot}nH_2O$ that has the anion clusters of $\{ClO_4^-\}_{10}$ with a dense structure requires a substantially higher temperature to induce a relaxer feature. It is worth mentioning that the cooperative dynamics is also crucial to the appearance of the quite large $\varepsilon'/\varepsilon_0$ values exceeding 10^5.

The presence of the cooperative dynamics due to inorganic anions and water molecules in the anionic cluster is also supported by the appearance of isotope and external pressure effects on the dielectric behaviour. As shown in Fig. 5b, the $\varepsilon'/\varepsilon_0$ values of the deuterated [**1**]$(NO_3)_2{\cdot}nD_2O$ are enhanced by nearly one order compared with those of the original sample of [**1**]$(NO_3)_2{\cdot}nH_2O$. A similar tendency was observed for the deuterated [**1**]$(SO_4){\cdot}nD_2O$ and [**1**]$(SiF_6){\cdot}nD_2O$ (Fig. S5). While [**1**]$Cl_2{\cdot}nD_2O$ does not show a drastic enhancement (Fig. 5c), the onset temperature is lower than that of [**1**]$Cl_2{\cdot}nH_2O$, suggesting a weak interaction of water molecules with Cl^- anions compared with the interaction with NO_3^- anions. These observations demonstrate that the dynamics of water molecules in [**1**]$X_2{\cdot}nH_2O$ is enhanced by the deuteration. Furthermore, the positive isotope effect observed here supports the importance of the dynamic features of water molecules to the appearance of the permittivity jump, considering that the weakening of hydrogen-bonding interactions in the cluster by the deuteration results in the increase of water molecule motion. Figure 5d shows the pressure and frequency dependences of $\varepsilon'/\varepsilon_0$ for [**1**]$Cl_2{\cdot}nH_2O$ at 350 K. The dielectric permittivity observed at ambient pressure is suppressed drastically with increasing pressure, and the increase of the dielectric permittivity is nearly completely suppressed above 0.7 GPa. It is reasonable to assume that the increase of external pressures causes the contraction of the anionic cluster space, preventing the dynamics of water molecules and inorganic anions needed for the appearance of a large dielectric permittivity.

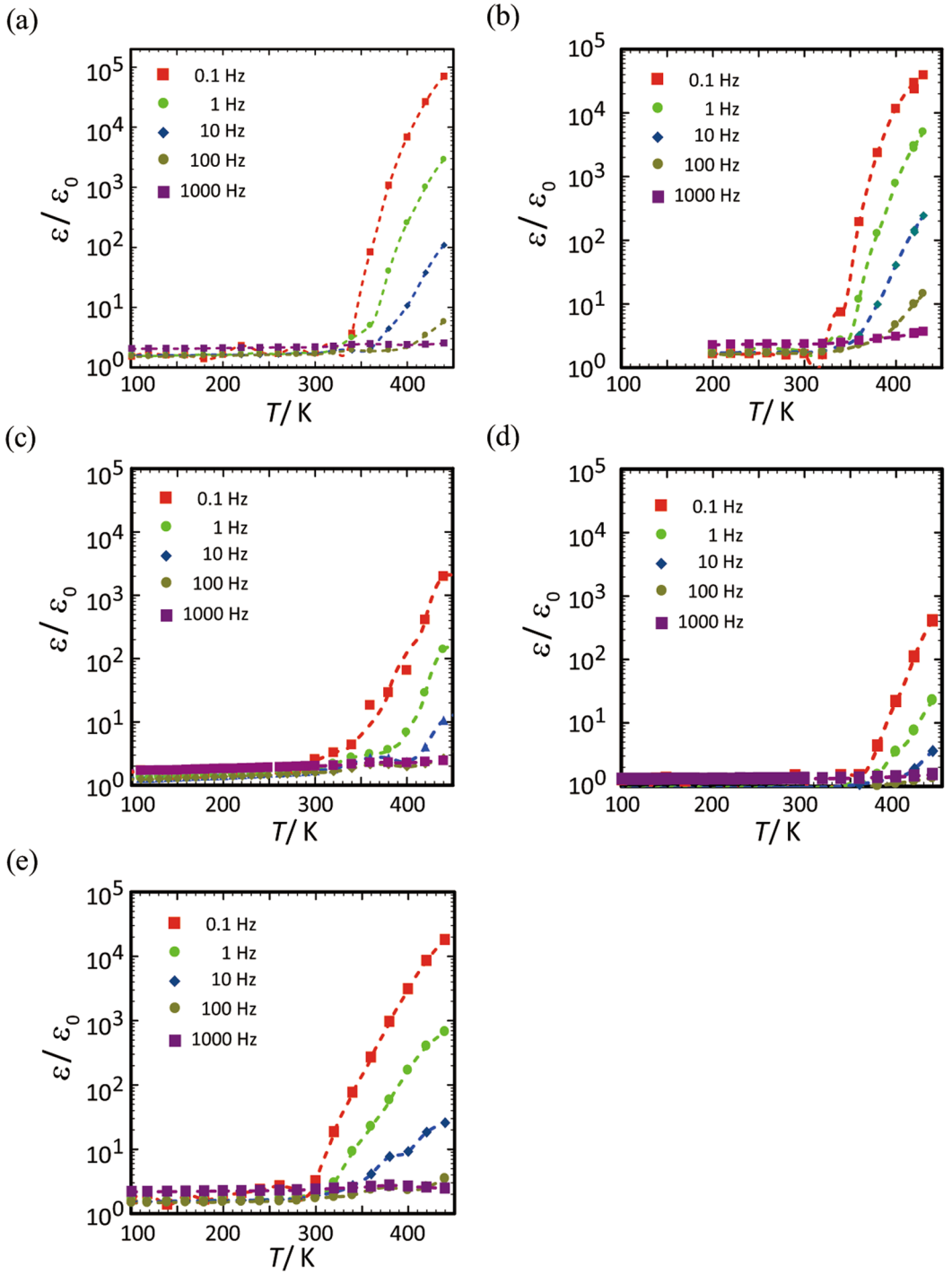

Figure 4. Temperature dependencies of $\varepsilon'/\varepsilon_0$ for (**a**) [**1**]$Cl_2{\cdot}nH_2O$, (**b**) [**1**]$Br_2{\cdot}nH_2O$, (**c**) [**1**]$(NO_3)_2{\cdot}nH_2O$, (**d**) [**1**]$(SO_4){\cdot}nH_2O$, and (**e**) [**1**]$(SiF_6){\cdot}nH_2O$.

We expected that the peculiar charge-separation state in the CS-NCISs of [**1**]$X_2{\cdot}nH_2O$ consisting of the cationic supramolecular octahedrons of $\{[\mathbf{1}]^{2+}\}_6$ and the anionic clusters of $\{X^-\}_{10}$ or $\{X^{2-}\}_6$ leads to the appearance of unusual charge-lattice coupling phenomena. Since the total charge valences of $\{[\mathbf{1}]^{2+}\}_6$ and $\{X^-\}_{10}$ or $\{X^{2-}\}_6$ are significantly larger than those of the cationic and anionic species in normal ionic solids[18], the application of a DC voltage seems to induce some strain in the crystal because of the opposite displacement of plus- and minus-charged cluster units by the electric field (Fig. 6a). To check this electrostriction effect, we carried out *Q-V* and *I-V* measurements for [**1**]$Cl_2{\cdot}nH_2O$ (Fig. 6b,c), which shows the largest dielectric jump among [**1**]$X_2{\cdot}nH_2O$ (Fig. 4). The crystal contraction/extension was also measured for [**1**]$Cl_2{\cdot}nH_2O$ by using AFM tips, with a sweeping DC voltage of up to $\pm 400\,V\,mm^{-1}$ (Fig. 6b,c). The *I-V* characteristic measured at 380 K shows a butterfly-type hysteretic feature, which is not observed at room temperature. Since the increase of current means a charging because of the increase

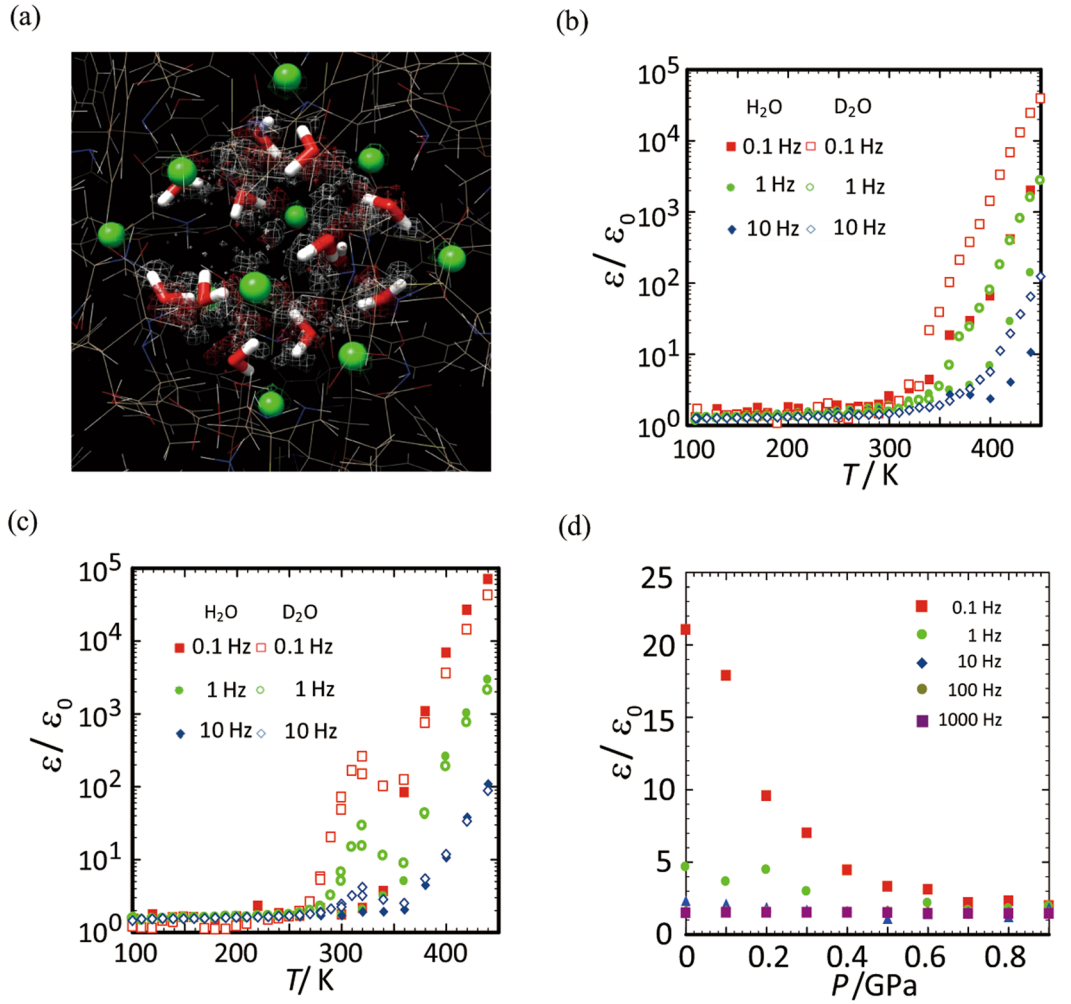

Figure 5. (**a**) Probability distributions of the inorganic-anion cluster in [**1**]$Cl_2 \cdot nH_2O$, obtained from QM/MM MD calculations at 300 K. The colours of the wire meshes for Cl, O, and H atoms are green, red, and white, respectively. The X-ray structure is also shown in the sphere (Cl^-) and the stick (H_2O) models. (**b**) Temperature dependencies of $\varepsilon'/\varepsilon_0$ for [**1**]$(NO_3)_2 \cdot nH_2O$ (closed symbol) and [**1**]$(NO_3)_2 \cdot nD_2O$ (open symbol) at 0.1 Hz, 1.0 Hz, and 10 Hz. (**c**) Temperature dependencies of $\varepsilon'/\varepsilon_0$ for [**1**]$Cl_2 \cdot nH_2O$ (closed symbol) and [**1**]$Cl_2 \cdot nD_2O$ (open symbol) at 0.1 Hz, 1.0 Hz, and 10 Hz. (**d**) External pressure dependencies of $\varepsilon'/\varepsilon_0$ for [**1**]$Cl_2 \cdot nH_2O$ at 350 K.

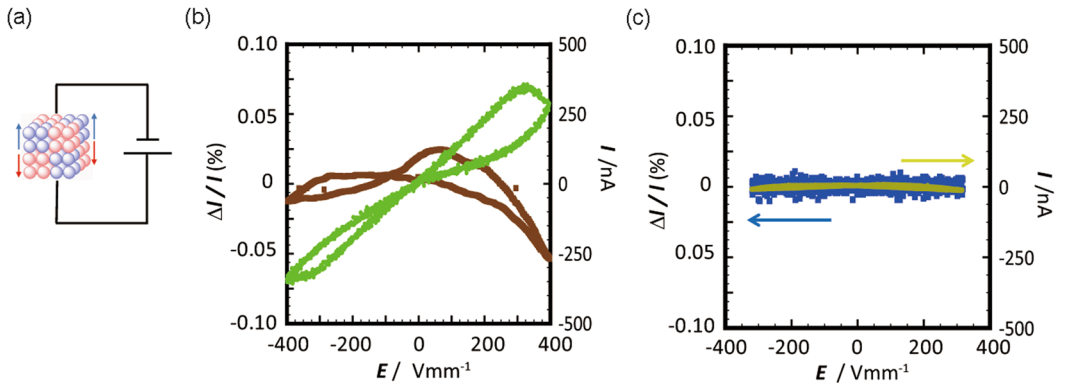

Figure 6. (**a**) Schematic illustration of the electrostriction effect. Simultaneous measurements of the *I-V* characteristics and the displacement of the sample position from the AFM tip at (**b**) 380 K and (**c**) room temperature.

of polarization produced by the deformation of the crystal lattice[18,19], the appearance of the hysteresis is attributed to an electrostriction. The electric contraction/extension was directly detected by using an AFM tip and simultaneous sweeping in the *I-V* measurements at 380 K, but not at room temperature (Fig. 6b). Thus, it is concluded that the electrostriction occurs synchronized with the electric charging in the crystal lattice at 380 K, while the changes in the polarization and displacement are not caused at room temperature. From the data in Fig. 6b, the relative value of the displacement, $\Delta l/l$, was evaluated to be 0.07% at 400 V mm^{-1}. This value is three times larger than that for PZT[18] and is comparable with the value for $BaTiO_3$, which was recently attained by the domain conversion technique[19]. More remarkably, the electrostriction effect occurs in the negative direction, that is, the crystal shrinkage occurs with increasing DC voltage applied to the crystal; although the charging feature is quite similar to that found in ceramics. Such an electrostriction with a negative displacement is unprecedented; normal electrostriction, as found in ceramics, is of positive displacement[18,19]. We also performed the crystal displacement measurements with increasing electric fields for a different, 10 times smaller sample. A similar, negative displacement feature was observed in both parallel and perpendicular directions (Fig. S6), although a slight difference was noticed between them. The crystal shrinkage with increasing DC voltage, which occurs in all *x*-, *y*-, and *z*-axes, was also recognized by the tracing of the Bragg spot positions and the refinement of the cell parameters in the single-crystal X-ray analysis of [**1**]Cl_2·$n$$H_2O$ (Fig. S7). These results imply that the total volume of crystalline [**1**]Cl_2·$n$$H_2O$ decreases with increasing voltage through the negative electrostriction. While the detailed mechanism of this negative electrostriction is not clear at present, we speculate that the removal of water molecules from the inorganic-anion clusters, which is induced by the strong striction and distortion by the electric field, leads to the shrinkage of the inorganic-anion clusters to contract the whole crystal that possesses a cubic lattice structure.

In summary, we succeeded in deriving remarkable dielectric features peculiar for CS-NCISs ([**1**]X_2·$n$$H_2O$) and discussed their mechanisms in terms of the soft dynamics of the anion clusters ($\{X^-\}_{10}$ or $\{X^{2-}\}_6$) triggered by water molecules accommodated in the clusters. We also found the unprecedented negative electrostriction for [**1**]Cl_2·$n$$H_2O$, which is induced by a DC bias application. These novel features for CS-NCISs should be explored for potential applications in sensing and/or vibration devices. The coexistence of robust cationic and soft anionic cluster regions in CS-NCIS is expected to lead to other novel functionalities based on the local non-equilibrium feature in a rigid crystal lattice, triggered by the activation of water molecules under non-wet conditions. We emphasize that NCISs might be a new generation of materials in which multiscale aspects coexist in the same crystal, as if in biological materials.

Methods

The synthesis of $[Au^I_4Co^{III}_2(dppe)_2(D\text{-}pen)_4]^{2+}$ and the growth of its single crystals with monovalent or divalent counteranions were performed according to the method reported in refs[2,3]. The diffraction data for [**1**]Cl_2·$n$$H_2O$ was recorded at 100 K with a RIGAKU/MSC Mercury CCD X-ray diffractometer with synchrotron radiation ($\lambda = 0.6889$ Å) at PF-AR (NW2A beamline) of the High Energy Accelerator Research Organization (KEK). The diffraction images were processed by using HKL2000. The diffraction data for [**1**]$(ClO_4)_2$, [**1**]$(NO_3)_2$, [**1**]Br_2, [**1**]SO_4 and [**1**]SiF_6 were recorded at 100 K with an ADSC Q210 CCD area detector with synchrotron radiation ($\lambda = 0.6500$ Å for [**1**]$(NO_3)_2$, [**1**]Br_2 and [**1**]SiF_6 and 0.7000 Å for [**1**]$(ClO_4)_2$, and [**1**]SO_4) at the 2D beamline at the Pohang Accelerator Laboratory (PAL). The intensity data were processed using the HKL3000 program, collected by using the ω-scan technique, and semi-empirically corrected for absorption by using PLATON. The diffraction data for [**1**]$(NO_3)_2$·$n$$D_2O$ were recorded at 300 K, 343 K and 423 K with a RIGAKU/Mercury 2 CCD detector with synchrotron radiation ($\lambda = 0.7003$ Å) at Spring-8 (BL02B1 beamline). The diffraction images were processed by using RAPID-AUTO. The tracing experiments of Bragg spots by X-ray diffraction with increasing DC voltages were performed with a RIGAKU/MSC Mercury CCD X-ray diffractometer with synchrotron radiation ($\lambda = 0.6889$ Å) at PF-AR (NW2A beamline) of the High Energy Accelerator Research Organization (KEK). The diffraction images of the single crystal ($0.25 \times 0.25 \times 0.15$ mm^3) of [**1**]Cl_2 with two lead wires (the sample was coated with epoxy) were recorded at 380 K. The diffraction images shown in Fig. S7 were collected by using the ω-scan technique ($\Delta\omega = 3$ °, exposure time = 3.0 sec) under both conditions without voltage and with 100 V. The cell parameters were determined after the refinements based on the 2321 for 0 V and 2124 for 100 V reflections in a ω range = 0–30 ° by using Crystal Clear 2.0. 0 V: Cubic F, $a = 37.6209(54)$ Å, $V = 53246\ (11)$ Å^3. 100 V: Cubic F, $a' = 37.5553(59)$ Å, $V' = 52968(12)$ Å^3.

The temperature and frequency dependencies of the ac impedance for [**1**]Cl_2·$n$$H_2O$ were measured by the Solartorn1260 system with the dielectric measurement interface 1296. The frequency range of the system is from 10^{-1} Hz to 10^5 Hz, and the temperature range is from 30 K to 440 K. The temperature of the sample part was controlled within ±0.1 K using the temperature controller LakeShore 335. Single crystals with a typical size of $0.4 \times 0.4 \times 0.2$ mm^3 were used for measurements by the four/two terminal method. A thin gold wire with a diameter of 30 μm was attached to a crystal using carbon paste (Fujikura DOTITE XC-12). To prevent the release of water of crystallization, the crystal surface was coated by an epoxy resin. The temperature dependence of the permittivity was calculated from the ac impedance using the formula of $Z''/C_0\omega Z^2$, where Z'', C_0, ω and Z are ideally part of the impedance, base capacitance of the set-up, frequency and measured impedance, respectively.

The polarization measurements with a DC electric voltage was performed on a FET-1E system (TOYO Cooperation) using the *Q-V*, *I-V* mode. A single crystal with two lead wires was coated by epoxy, to ensure the contact of the current leads on the crystal and to prevent the release of water molecules in the dry atmosphere. The simultaneous measurements of the polarization and displacement of the crystal by sweeping electric voltage were performed by the combined FET-1E with AFM measurements. The temperatures of the sample stage were controlled to within ±1.0 K using a chip-type Pt sensor.

The numerical studies were performed by quantum mechanics (QM)/molecular mechanics (MM) MD simulation methods. The simulation was performed with Amber14. The details of the model and calculation procedures are explained in the supporting information (Fig. S8). The validity of the liquid-like feature of water molecules was discussed through the comparison with the ab initio QM result (Figs S8, S9).

Accession codes. The X-ray crystallographic coordinates for the structure reported in this Article have been deposited at the Cambridge Crystallographic Data Centre (CCDC) under deposition number CCDC 1578196–1578204. These data can be obtained free of charge from the Cambridge Crystallographic Data Centre via www.ccdc.cam.ac.uk/data_request/cif.

References

1. Yoshinari, N. & Konno, T. Metallosupramolecular structures derived from a series of diphosphine-bridged digold(I) metalloligands with terminal d-Penicillamine. *Chem. Rec.* **16**, 1647–1663 (2016).
2. Lee, R., Igashira-Kamiyama, A., Okumura, M. & Konno, T. Extraordinary aggregation of inorganic anions in chiral metallosupramolecular ionic crystals. *Bull. Chem. Soc. Jpn.* **86**, 908–920 (2013).
3. Lee, R., Igashira-Kamiyama, A., Motoyoshi, H. & Konno, T. Aggregation of chiral hexanuclear complex-cations into cationic metallosupramolecules with concomitant aggregation of inorganic counter-anions into anionic clusters. *Cryst Eng Comm* **14**, 1936–1938 (2012).
4. Igashira-Kamiyama, A. & Konno, T. Rational creation of chiral multinuclear and metallosupramolecular compounds from thiol-containing amino acids. *Dalton Trans.* **40**, 7249–7263 (2011).
5. von Hippel, A. *Dielectric materials and applications* (Artech House, Boston 1954).
6. Brown, W. F. Jr. *Dielectrics*, (Springer, Berlin, 1956).
7. Lines, M. E. & Glass, A. M. *Principles and applications of ferroelectric and related materials* (Oxford University Press, New York 1977).
8. Torrance, J. B., Vazquez, J. E., Mayerle, J. J. & Lee, V. Y. Discovery of a neutral-to-ionic phase transition in organic materials. *Phys. Rev. Lett.* **46**, 253–257 (1981).
9. Horiuchi, S., Kumai, R., Okimoto, Y. & Tokura, Y. Chemical approach to neutral–ionic valence instability, quantum phase transition, and relaxor ferroelectricity in organic charge-transfer complexes. *Chem. Phys.* **325**, 78–91 (2006).
10. Raengthon, N. & Camn, D. P, Dielectric relaxation in $BaTiO_3$-$Bi(Zn_{1/2}Ti_{1/2})O_3$. *J. Am. Ceram. Soc.* **95**, 1604–1612 (2011).
11. Zhao, X., Qu, W., Tan, X., Bokov, A. A. & Ye, Z.-G. Influence of long-range cation order on relaxer properties of doped $Pb(Mg_{1/3}Nb_{2/3})O_3$ ceramics, *Phys. Rev. B* **79**(144101), 1–12 (2009).
12. Velikov, V., Borick, S. & Angell, C. A. The glass transition of water, based on hyperquenching experiments. *Science* **294**, 2385–2338 (2001).
13. Oguni, M., Kanke, Y., Nagoe, A. & Namba, S. Calorimetric study of water glass transition in nanoscale confinement suggesting a value of 210 K for bulk water, *J. Phys. Chem. B* **114**, 13940–13943 (2010).
14. Oguni, M., Maruyama, S., Wakabayashi, K. & Nagoe, A. Glass transition of ordinary and heavy water within silica-gel nanopores. *Chem. Asian. J.* **2**, 514–520 (2007).
15. Banys, J. *et al*. Broadband dielectric spectroscopy of water confined in MCM-41 molecular sieve materials—low-temperature freezing phenomena. *J. Phys.: Condens Matter* **17**, 14023–14029 (2011).
16. Zhou, B. *et al*. Anomalous Dielectric behaviour and thermal motion of water molecules confined in channels of porous coordination polymer crystals. *J. Am. Chem. Soc.* **133**, 5736–5739 (2011).
17. Zhao, H.-X. *et al*. Transition from one-dimensional water to ferroelectric ice within a supramolecular architecture. *PNAS* **108**, 3481–3486 (2011).
18. Uchino, K. *Ferroelectric Devices*, (Marcel Dekker, Inc. NewYork, 2000).
19. Ren, X. Large electric-field-induced strain in ferroelectric crystals by point-defect-mediated reversible domain switching. *Nature Mat.* **3**, 91–94 (2004).

Acknowledgements

This work was financially supported by CREST, JST program in the area of "Establishment of Molecular Technology towards the Creation of New Functions" (Grant No. JPMJCR13L3). We thank to Dr. Someya and Dr. Komori (TOYO Cooperation) for their technical supports for the electrostriction measurements. The synchrotron radiation experiments were performed at the BL02B1 of SPring-8 with the approval of the Japan Synchrotron Radiation Research Institute (JASRI) (Proposal No. 2015B1001, and 2014B1022), at NW2A of PF-AR with the approval of the Photon Factory Program Advisory Committee (Proposal No. 2014G008) and at 2D-SMC of Pohang Accelerator Laboratory.

Author Contributions

N.Y. and T.K. worked on the synthesis and the characterizations of the single crystal samples. S.Y. and Y.N. conducted the heat capacity, the ac impedance, and the electrostriction measurements. S.Y. and M.O. performed theoretical calculations. T.K. designed the research plan and worked on the overall discussions throughout the project. S.Y., Y.N. and T.K. mainly wrote the manuscript, and all authors discussed the results and commented on the manuscript.

Additional Information

Supplementary information accompanies this paper at https://doi.org/10.1038/s41598-018-20750-1.

Competing Interests: The authors declare no competing interests.

Publisher's note: Springer Nature remains neutral with regard to jurisdictional claims in published maps and institutional affiliations.